

Magnet-Free Time-Resolved Magnetic Circular Dichroism with Pulsed Vector Beams

Jiaan Cao,[#] Lyuzhou Ye,^{*,#} Dawei He, Xiao Zheng,^{*} and Shaul Mukamel



Cite This: *J. Phys. Chem. Lett.* 2022, 13, 11300–11306



Read Online

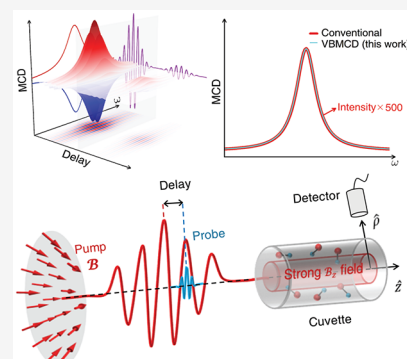
ACCESS |

Metrics & More

Article Recommendations

Supporting Information

ABSTRACT: Magnetic circular dichroism (MCD) is a widely used spectroscopic technique which reveals valuable information about molecular geometry and electronic structure. However, the weak signal and the necessary strong magnets impose major limitations on its application. We propose a novel protocol to overcome these limitations by using pulsed vector beams (VBs), which consist of nanosecond gigahertz pump and femtosecond UV-vis probe pulses. By virtue of the strong longitudinal electromagnetic fields, the MCD signal detected by using the pulsed VBs is greatly enhanced compared to conventional MCD performed with plane waves. Furthermore, varying the pump–probe time delay allows monitoring the ultrafast variation of molecular properties.



Over the past decades, magnetic molecules, ranging from simple radicals to single molecule magnets, have opened up potential applications in many areas, such as molecular spintronics,^{1–3} magnetic refrigeration,^{4–7} and electrocatalysis.^{8,9} Various optical spectroscopic techniques have been developed to investigate the electronic and magnetic properties of molecules and understand the magneto-structural correlation, and magnetic circular dichroism (MCD) is one of the most widely used tools.^{10–12} In this technique, a strong static magnetic field is applied to induce Zeeman splitting in molecules by lifting the degeneracy of the electronic states.^{13,14} The MCD signal is then given by the differential absorption of the left- and right-circularly polarized (LCP and RCP) light passing through the molecular sample.¹⁰ MCD has demonstrated its superiority over linear absorption spectroscopy in determining electronic transitions,^{13,15,16} as well as in revealing information about the degeneracy and symmetry of electronic states.^{10,12,17} Despite its rapid progress and wide applications, MCD still faces several challenges: First is the differential absorption of the LCP and RCP plane waves (PWs). The intensity of the conventional MCD signal is generally 2 to 3 orders of magnitude weaker than that of the absorption signal.^{18–21} Second, a strong static magnetic field is needed to induce the Zeeman splitting in conventional MCD experiments. Although numerous types of magnets have been designed,^{10,13,22} their practical use can be cumbersome, because of the required large-sized devices and cryogenic temperatures.^{10,22–24}

The first challenge concerning a weak signal can be overcome by replacing the LCP and RCP PWs by left- and right-circularly polarized beams with nonzero longitudinal

components (LCPL and RCPL),²⁵ which are realized by superposing the azimuthally and radially polarized (AP and RP) vector beams (VBs). It has been proposed that VBs could greatly enhance the circular dichroism (CD) signals of chiral molecules,²⁵ thanks to the strong electromagnetic fields generated by the VBs. However, it is difficult to probe time-varying molecular properties with continuous-wave VBs, which raises a third challenge for MCD measurements.

Inspired by the recent progress in the design and implementation of VBs^{19,26–28} and gigahertz (GHz) spectroscopy,^{29,30} in this work we propose a novel protocol for magnet-free time-resolved MCD measurements, which utilizes pulsed VBs and will be denoted VBMCD.

VBS have cylindrical symmetry along the beam axis. In the cylindrical coordinate system, the electric and magnetic fields of a pulsed AP VB are expressed as

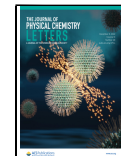
$$\mathcal{E}_{\text{AP}}(\mathbf{r}, t) = \hat{\phi} \mathcal{H}(\mathbf{r}) e^{i(Kz - \Omega t)} \mathcal{G}(t) \quad (1)$$

$$\mathcal{B}_{\text{AP}}(\mathbf{r}, t) = \left[\hat{\rho} \left(-\frac{K}{\Omega} \right) + \hat{z} \left(-\frac{i}{\Omega} \right) \left(\frac{1}{\rho} + \frac{\partial}{\partial \rho} \right) \right] \mathcal{H}(\mathbf{r}) e^{i(Kz - \Omega t)} \mathcal{G}(t) \quad (2)$$

Received: November 7, 2022

Accepted: November 28, 2022

Published: November 30, 2022



ACS Publications

© 2022 American Chemical Society

Here, $\hat{\rho}$, $\hat{\phi}$, and \hat{z} represent the radial, azimuthal, and longitudinal unit vectors, respectively; $\mathbf{r} \equiv (\rho, \phi, z)$, and Ω is the central frequency. The spatial profile assumes a Hermite-Gaussian form,²⁶

$$\mathcal{H}(\mathbf{r}) = \mathcal{A}_0 \frac{4\rho}{\sqrt{\pi} [W(z)]^2} \exp\left[-\frac{\rho^2}{[W(z)]^2}\right] \exp\left[\frac{iK\rho^2}{2R(z)}\right] \exp\left[-2i \arctan\left(\frac{z}{z_R}\right)\right] \quad (3)$$

where \mathcal{A}_0 is the amplitude, K is the wavenumber, W_0 is the beam waist, $z_R = \frac{1}{2}KW_0^2$ is the Rayleigh length, $W(z) = W_0\sqrt{1+z^2/z_R^2}$ is the beam width, and $R(z) = z + z_R^2/z$ is the radius of curvature. The temporal profile assumes a Gaussian form,

$$\mathcal{G}(t) = \exp\left[-4 \ln 2 \frac{(t - T_c)^2}{\tau_D^2}\right] \quad (4)$$

with T_c and τ_D being the central time and the duration time, respectively. The corresponding electric and magnetic fields of the pulsed RP VB are respectively²⁶

$$\mathcal{E}_{\text{RP}}(\mathbf{r}, t) = \left[\hat{\rho} + \hat{z} \left(\frac{i}{K} \left(\frac{1}{\rho} + \frac{\partial}{\partial \rho} \right) \right) \mathcal{H}(\mathbf{r}) e^{i(Kz - \Omega t)} \mathcal{G}(t) \right] \quad (5)$$

$$\mathcal{B}_{\text{RP}}(\mathbf{r}, t) = \hat{\phi} \left(\frac{K}{\Omega} \right) \mathcal{H}(\mathbf{r}) e^{i(Kz - \Omega t)} \mathcal{G}(t) \quad (6)$$

In this work the 0.1–10 T static magnetic field typically used in conventional MCD is replaced by a temporally- and spatially-varying magnetic field $\mathcal{B}(\mathbf{r}, t) = \mathcal{B}_{\text{AP}}(\mathbf{r}, t)$, which is generated by an AP VB (Figure 1a). The longitudinal component of \mathcal{B}_{AP} , denoted as \mathcal{B}_z , is tightly localized around the beam axis, and its amplitude decreases rapidly with the radial distance ρ (Figure 1b).^{26–28} To create an appreciable Zeeman splitting in the molecule, a pulsed VB is utilized as the pump beam to supply a strong longitudinal field \mathcal{B}_z . Two pulsed probe beams, LCPL

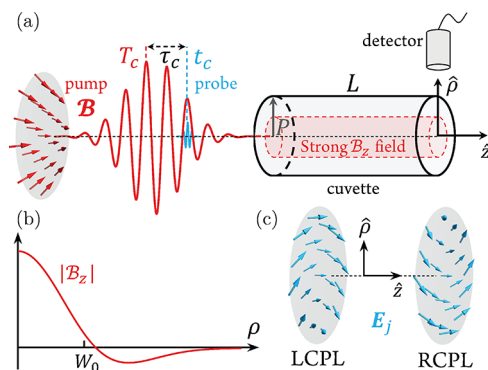


Figure 1. (a) Schematic of the proposed VBMCD protocol. The red cylinder represents the paraxial region where a strong localized magnetic field exists. $\hat{\rho}$ and \hat{z} denote the radial and longitudinal directions, and T_c and t_c are the centers of pump and probe pulses, respectively. (b) Variation of $|\mathcal{B}_z|$ with respect to ρ , where W_0 is the pump beam waist. (c) Vector field plots of the LCPL and RCPL probe VBs.

and RCPL²⁵ (Figure 1c), which are collinear with the pump VB, are employed to measure the MCD signals. The electric and magnetic fields of the probe pulses are explicitly expressed as²⁵

$$\begin{pmatrix} \mathbf{E}_j(\mathbf{r}, t) \\ \mathbf{B}_j(\mathbf{r}, t) \end{pmatrix} = \frac{-1}{\sqrt{2}} \begin{pmatrix} \mathbf{E}_{\text{AP}}(\mathbf{r}, t) & \mathbf{E}_{\text{RP}}(\mathbf{r}, t) \\ \mathbf{B}_{\text{AP}}(\mathbf{r}, t) & \mathbf{B}_{\text{RP}}(\mathbf{r}, t) \end{pmatrix} \begin{pmatrix} c_j \\ i \end{pmatrix} \quad (7)$$

where $c_j = 1$ for $j = \text{LCPL}$ and -1 for $j = \text{RCPL}$, and $\mathbf{E}_{\text{AP/RP}}$ and $\mathbf{B}_{\text{AP/RP}}$ denote the electric and magnetic fields of the AP/RP VBs for designing the LCPL and RCPL, respectively. The spatial and temporal profiles of the probe VBs, denoted as $H(\mathbf{r})$ and $G(t)$, have the same forms as those of the pump, but the values of the involving parameters are different. These include amplitude A_0 , wavenumber k_j , beam waist w_0 , pulse central time t_c and duration time τ_d .

To ensure that the Zeeman states are detectable by the probe VBs, the strength of localized magnetic field should reach 0.1–10 T.¹³ Moreover, to acquire a nonzero time-averaged MCD signal with the oscillatory pump pulse, the duration of the probe pulses should be much shorter than that of the pump pulse, so that the longitudinal magnetic field \mathcal{B}_z of the pump beam is almost unchanged during the action of the probe pulse. These suggest the use of a nanosecond GHz pump pulse and femtosecond UV-vis probe pulses. Generation of such pulsed VBs is well within the capabilities of current technology.^{28–30} Furthermore, the time delay between the pump and probe pulses can be precisely tuned, thus allowing for the detection of time-varying molecular properties.

In the following, we compare the VBMCD signal to conventional MCD. The light-matter interaction Hamiltonian for our setup is

$$H_{\text{int}} = -\hat{\mu} \cdot \mathbf{E}_j - \hat{m} \cdot \mathcal{B} - \frac{1}{2} \hat{Q} : \nabla \mathbf{E}_j + \text{H.c.}$$

where $\hat{\mu}$, \hat{m} , and \hat{Q} are the electric transition dipole, magnetic transition dipole, and electric transition quadrupole operators, respectively. The contribution of the electric quadrupole term to the MCD signal vanishes when rotational averaging is performed over randomly oriented molecules in solutions or in the gas phase.^{10,31} The interactions between the molecular transition dipoles and the electric component of the pump VB and the magnetic component of the probe pulses are neglected, because the former is off-resonant with the electronic excitations in molecules due to much lower frequency of the pump pulse, while the latter is several orders of magnitude weaker than $-\hat{\mu} \cdot \mathbf{E}_j$.¹⁰

The wavenumber k_j of the LCPL and RCPL pulses can be obtained by first-order time-dependent perturbation theory;³² see Section S1 in the Supporting Information (SI). Their difference, $\Delta k \equiv k_{\text{LCPL}} - k_{\text{RCPL}}$, which largely determines the line shape of the MCD spectrum, is expressed as the sum of three Faraday terms, denoted by $A(\omega)$, $B(\omega)$, and $C(\omega)$, as follows,

$$\Delta k(\omega) = \frac{n\mu_0 c}{3\hbar^2} \mathcal{B}_z(\mathbf{r}, t) [A(\omega) + B(\omega) + C(\omega)] \quad (8)$$

$$\Lambda(\omega) = \tilde{\Lambda}(\omega, \Omega) + \frac{\mathcal{B}_z^*(\mathbf{r}, t)}{\mathcal{B}_z(\mathbf{r}, t)} \tilde{\Lambda}(\omega, -\Omega), \quad (9)$$

$$\Lambda \in \{A, B, C\}$$

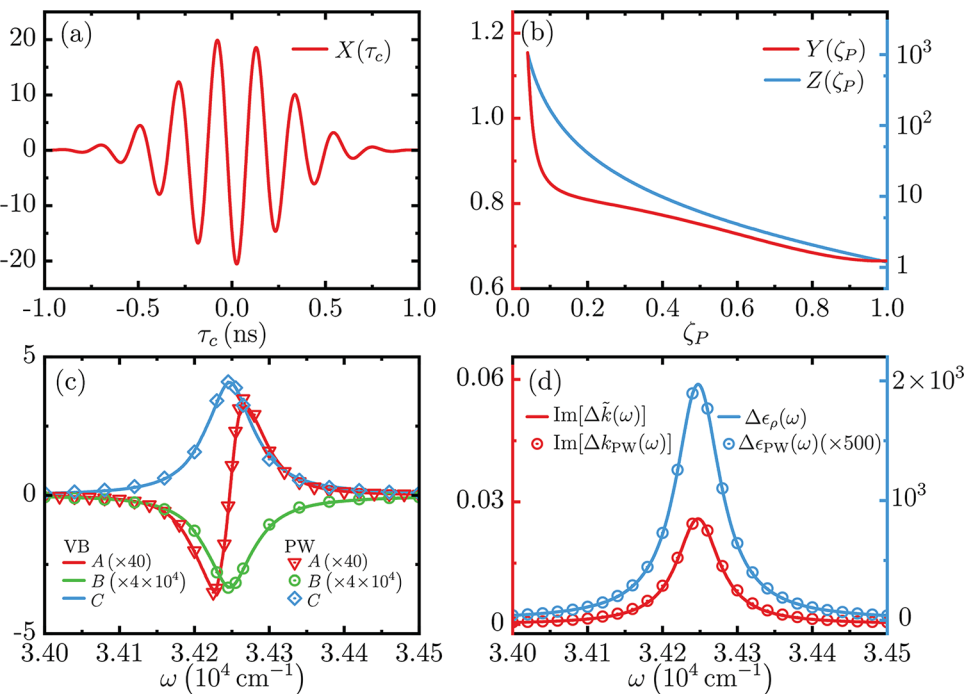


Figure 2. Characteristic functions which determine the intensity of the VBMCD spectrum: (a) $X(\tau_c)$ and (b) $Y(\zeta_P)$ and $Z(\zeta_P)$. (c) The Faraday A , B , and C terms of the VBMCD and the conventional MCD with PWs for the $\cdot\text{OH}$ radical. (d) $\text{Im}[\Delta\tilde{k}(\omega)]$ versus $\text{Im}[\Delta k_{\text{PW}}(\omega)]$ (left axis), and $\Delta\epsilon_\rho(\omega)$ versus $\Delta\epsilon_{\text{PW}}(\omega)$ (right axis) for the $\cdot\text{OH}$ radical. For a direct comparison, $\Delta\epsilon_{\text{PW}}(\omega)$ is amplified manually by 500 times. The parameters adopted for the simulations are listed in sections S2 and S3 in the SI. The molecular properties are obtained from quantum chemistry calculations^{33–37} by using the ORCA³⁸ and the MOLCAS³⁹ program packages.

$$\bar{A}(\omega; \Omega) = \frac{i(\omega + \Omega)^2}{2N_g\omega} \sum_{g_\alpha, l_\beta} \sum_{g_{\alpha'}, l_{\beta'}} \frac{\partial f_{l_\beta g_\alpha}(\omega)}{\partial \omega} \\ (\mathbf{m}_{l_\beta l_{\beta'}} \delta_{g_\alpha g_{\alpha'}} - \mathbf{m}_{g_\alpha g_{\alpha'}} \delta_{l_\beta l_{\beta'}}) \cdot (\mathbf{\mu}_{g_\alpha l_{\beta'}} \times \mathbf{\mu}_{l_\beta g_\alpha}) \quad (10)$$

$$\begin{aligned} \bar{B}(\omega; \Omega) = & \frac{-i(\omega + \Omega)^2}{2N_g\omega} \sum_{g_\alpha, l_\beta} [f_{l_\beta g_\alpha}(\omega) + f_{l_\beta g_\alpha}(\omega + \Omega)] \\ & \left[\sum_{v_\gamma, v_\gamma \neq g_\alpha} \frac{(\mathbf{\mu}_{l_\beta g_\alpha} \times \mathbf{\mu}_{v_\gamma l_\beta}) \cdot \mathbf{m}_{g_\alpha v_\gamma}}{\Omega + \omega_{v_\gamma g_\alpha}} \right. \\ & \left. + \sum_{v_\gamma, v_\gamma \neq l_\beta} \frac{(\mathbf{\mu}_{g_\alpha v_\gamma} \times \mathbf{\mu}_{l_\beta g_\alpha}) \cdot \mathbf{m}_{v_\gamma l_\beta}}{\Omega + \omega_{l_\beta v_\gamma}} \right] \quad (11) \end{aligned}$$

$$\begin{aligned} \bar{C}(\omega; \Omega) = & \frac{-i(\omega + \Omega)^2}{2N_g\omega} \frac{\hbar}{k_B T} \sum_{g_\alpha, g_{\alpha'}, l_\beta} f_{l_\beta g_\alpha}(\omega + \Omega) \\ & (\mathbf{\mu}_{l_\beta g_\alpha} \times \mathbf{\mu}_{g_{\alpha'} l_\beta}) \cdot \mathbf{m}_{g_\alpha g_{\alpha'}} \quad (12) \end{aligned}$$

Here, n is the molecular concentration, μ_0 is the magnetic permeability, c is the speed of light, and

$$f_{l_\beta g_\alpha}(\omega) \equiv (\omega - \omega_{l_\beta g_\alpha} + i\eta)^{-1}$$

with g_α and l_β labeling the states in the degenerate sublevels of the ground (g) and excited (l) states, respectively. T is the temperature, N_g is the degeneracy of the ground state manifold, $\mu_{l_\beta g_\alpha}$ and $\mathbf{m}_{l_\beta g_\alpha}$ denote the electric and magnetic transition dipole moments between states l_β and g_α respectively. The

expressions in eqs 10–12 reduce to their counterparts for the conventional MCD when the pump central frequency $\Omega = 0$. Therefore, the conventional MCD spectrum measured with PW beams can be recovered by replacing \mathcal{B}_z with a static magnetic field B_z (section S1 in the SI).

The Faraday A , B , and C terms in eq 8 are functions of the probe central frequency ω . They provide valuable information about the degeneracy and symmetry of electronic states. Specifically, the A term arises from the Zeeman splitting of orbitally degenerate excited states. It has a characteristic derivative line shape and is independent of temperature. The B term originates from the magnetic-field-induced mixing of the zero-field nondegenerate states. It is also temperature-independent, but usually much smaller compared to the other two terms. The C term exhibits a strong inverse-temperature dependence. It reveals the information about the ground state population in the presence of the Zeeman splitting due to the external magnetic field, and is nonvanishing only for molecules with degenerate ground states.^{10,13,14}

For a PW beam, the longitudinal components of electric and magnetic fields are absent, and thus the luminous flux (magnitude of Poynting vector) is entirely along the axial direction of beam. Consequently, the flux can be gathered only in the longitudinal direction for the conventional MCD. In contrast, VBs have strong longitudinal components of electric and magnetic fields, and the luminous flux is nonzero in the radial direction. By using a cylindrical sample cuvette aligned coaxially with the probe pulses (Figure 1a), the luminous flux in the radial direction, gathered by the detector placed at a given azimuthal angle ϕ , is

$$I_p(\omega, \tau_c; k_j) = \frac{1}{\mu_0} \int dt \int_0^P \rho \mathbf{E}_j \times \mathbf{B}_j^* \cdot d\rho + c.c.$$

with P being the radius of interaction cross section between the probe beams and the molecular sample. Because of their cylindrical symmetry, both \mathbf{E}_j and \mathbf{B}_j are independent of ϕ , and hence the luminous flux $I_p(\omega, \tau_c; k_j)$ detected at any ϕ is identical. Therefore, using a ring-like detector encircling the axis of cuvette is most favorable for the collection of luminous flux.

The linear absorption spectrum is

$$\epsilon_p(\omega, \tau_c; k_j) = (n_0 L)^{-1} \ln[I_p(\omega, \tau_c; k_0)/I_p(\omega, \tau_c; k_j)]$$

where τ_c is the time delay between the pump and probe pulses, n_0 is a reference molecular concentration, L is the length of the sample cuvette, and $k_0 = \omega/c$ is the wavenumber of the probe VBs in vacuum. The resulting VBMCD spectrum is explicitly expressed as

$$\begin{aligned} \Delta\epsilon_p(\omega, \tau_c) &\equiv \epsilon_p(\omega, \tau_c; k_{LCPL}) - \epsilon_p(\omega, \tau_c; k_{RCPL}) \\ &= \frac{1}{n_0 L} \ln \left[\frac{I_p(\omega, \tau_c; k_{RCPL})}{I_p(\omega, \tau_c; k_{LCPL})} \right] \end{aligned} \quad (13)$$

Clearly, the VBMCD spectroscopic signal characterizes the difference between the linear absorption spectra measured by the LCPL and RCPL beams, rather than their absolute amplitudes. Thus, the intensity of the VBMCD signal should be distinguished from that of luminous flux collected by the detector. Particularly, although the luminous flux in the radial direction is relatively weaker than in the longitudinal direction, it is sufficiently bright to be harvested by modern detectors. Therefore, the VBMCD signal can be significantly enhanced over that of the conventional MCD, even with a relatively weaker luminous flux received by the detector.

To elucidate the origin of signal enhancement, we express the VBMCD spectrum $\Delta\epsilon_p$ as

$$\Delta\epsilon_p(\omega, \tau_c) \simeq \frac{\text{Im}[\Delta\tilde{k}(\omega)]}{n_0} \frac{X(\tau_c)Y(\zeta_p)Z(\zeta_p)}{2\zeta_L^2} \quad (14)$$

Here, $\zeta_L \equiv L/w_0$ and $\zeta_p \equiv P/w_0$ are the reduced path length and reduced radius of the cuvette, respectively, with w_0 being the probe beam waist. $\Delta\tilde{k}(\omega)$ is $\Delta k(\omega)$ evaluated at $\tau_c = 0$ and $\rho = W_0$. It dominates the line shape of the VBMCD spectrum, which resembles closely the conventional MCD spectrum. $X(\tau_c)$, $Y(\zeta_p)$, and $Z(\zeta_p)$ are three characteristic functions which determine the intensity of the measured spectrum (see section S1 in the SI for more details). They are independent of the molecular details. Specifically, $X(\tau_c)$ is a time-varying function whose temporal profile is almost identical to that of the pump pulse (see Figures 1a and 2a). $Y(\zeta_p)$ and $Z(\zeta_p)$ are enhancement factors which originate from the strong longitudinal electromagnetic fields generated by the pump and the probe VBs, respectively. Particularly, the Z factor increases drastically with the decrease of ζ_p (Figure 2b). Moreover, the intensity of the VBMCD signal is inversely proportional to the quadratic of ζ_L . Therefore, using a shorter and thinner sample cuvette is generally more favorable to achieve an enhanced VBMCD spectrum. Nevertheless, in practice the sample cuvette cannot be too small, because too few molecules could make the luminous flux in the radial

direction too weak to detect or the signal-to-noise ratio too low.

To demonstrate the utility of the proposed VBMCD protocol, we perform simulations for the MCD signals of the hydroxyl ($\cdot\text{OH}$) radical (section S2 in the SI). Figure 2c and 2d depict the line shape and intensity of the VBMCD spectrum, which are compared in parallel with the conventional MCD spectrum [$\Delta\epsilon_{PW}(\omega)$] probed by PWs (see eq S12 in the SI for more details). The Faraday A , B , and C terms of the VBMCD spectrum agree closely with their counterparts of the conventional MCD spectrum. This confirms that the VBMCD protocol reproduces all the important spectroscopic information rendered by conventional MCD.

By definition, it is clear that the signal acquisition time does not affect the magnitude of absorption or MCD spectra, but does affect the signal-to-noise ratio in an experiment. Hence, in order to compare the VBMCD and conventional MCD spectra on an equal basis and to accentuate the importance of the enhancement factors, in our simulations we assume that all measurements are performed with sufficiently high signal-to-noise ratio with long enough acquisition time and that the VBs and PWs are equally affected by the optical elements (not shown in Figure 1). In Figure 2d, the localized magnetic field \mathcal{B}_z generated by the pump pulse has a peak value of 0.74 T, about 10 times weaker than the static magnetic field B_z (~ 7.4 T) adopted for the conventional MCD. However, it is remarkable to see that the intensity of $\Delta\epsilon_p(\omega)$ is 500 times stronger than that of the conventional MCD $\Delta\epsilon_{PW}(\omega)$. Although the intensity of both VBMCD signal and conventional MCD signal scales linearly with the magnetic field (see eq 8 and section S1 in the SI), the radially detected VBMCD signal can be considerably enhanced by properly adjusting the enhancement factors in eq 14, which is not possible for the conventional MCD. These results verify that the enhancement factors associated with the radial detection scheme cause the significant enhancement of the VBMCD signal in Figure 2d. Moreover, a pulsed VB is superior to a continuous-wave VB as the pump, since the former can yield a stronger transient magnetic field by consuming the same amount of power. It is possible to further enhance the VBMCD signal by tailoring the VBs. For instance, by aiming the AP VB to a metallic circular aperture,²⁷ the amplitude of \mathcal{B}_z can be further amplified by ~ 3.8 times, reaching a peak value of 2.8 T (see section S1 in the SI for more details). Specifically, by setting the probe beam waist, and the radius and length of the sample cuvette to $w_0 = 1$ mm, $P = 0.1$ mm and $L = 0.03$ mm,⁴⁰ respectively, the VBMCD signal will reach an intensity about 4 orders of magnitude stronger than the conventional MCD.

Pulsed VBs enable a magnet-free experimental protocol and achieve a substantial enhancement of MCD signals, and further allow for the detection of real-time dynamics of molecular systems by tuning the time delay between the pump and probe pulses. In the present time-resolved VBMCD protocol, the pump pulses do not trigger any dynamic change of molecules. Instead, they impose weak perturbation on the molecular electronic states by creating Zeeman splitting, so that the molecules become discernible to the subsequent probe pulses.

As a demonstration, we consider two scenarios, in which $\cdot\text{OH}$ radicals are consumed or produced at the nanosecond time scale, respectively. The corresponding time-resolved VBMCD spectra, $\Delta\epsilon_p(\omega, \tau_c)$, are displayed in Figure 3a and 3b. In each scenario, two temporally separated pump pulses are

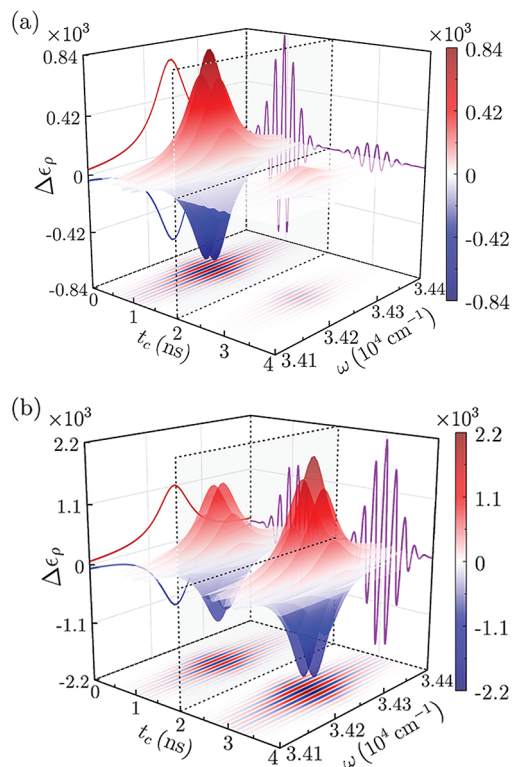


Figure 3. Simulated time-resolved VBMCD spectra of ·OH radicals, $\Delta\epsilon_r(\omega, \tau_c)$, in two scenarios characterized by the time-varying molecular concentration: (a) $n(t) = n_0 e^{-rt}$ and (b) $n(t) = n_0(1 - e^{-rt})$, with the rate constant $r = 1 \text{ ns}^{-1}$. Both scenarios adopt two temporally separated pump pulses centered at $T_c = 1 \text{ ns}$ and 3 ns , and the vertical plane at $t = 2 \text{ ns}$ (indicated by dashed lines) marks the center of interval between the two pump pulses. Note that the time delay has been converted to the probe central time, i.e., $t_c = T_c + \tau_c$. The other parameters adopted for the simulations are listed in section S3 in the SI.

applied, and the relative intensities of the MCD signal detected at the probe central time t_c directly reflect the change in molecular concentration over time, since $\Delta\epsilon_r \propto n(t)$. The signal changes its sign periodically with t_c due to the $X(\tau_c)$ factor in eq 14, and the signal intensity reaches its maximum when the pump–probe time delay is zero, because the corresponding pump magnetic field is the strongest. In Figure 3a, the signal intensity is much reduced at the second pump pulse, which reveals a rapid drop in concentration; whereas in Figure 3b, the signal is somewhat enhanced at the second pump pulse, indicating a mild increase in concentration.

As inferred from eqs 8 and 14, the time dependence of the VBMCD spectra is governed by the molecular concentration $n(t)$ and the pump magnetic field $\mathcal{B}_z(r, t)$, and the parameters for the latter are already known and can be precisely controlled when conducting an experiment. Therefore, by performing the calculation for $\Delta\epsilon_r(\omega, \tau_c)/\mathcal{B}_z(r, t)$, we can extract the time-dependent molecular concentration from the measured VBMCD spectra. As exemplified in Figure 4, the calculated data for the ·OH radical consumption and production processes (Figure 3) agree closely with the actual concentrations. Hence, the time-resolved VBMCD signal provides a route to extract information about the real-time variation of the molecular concentration.

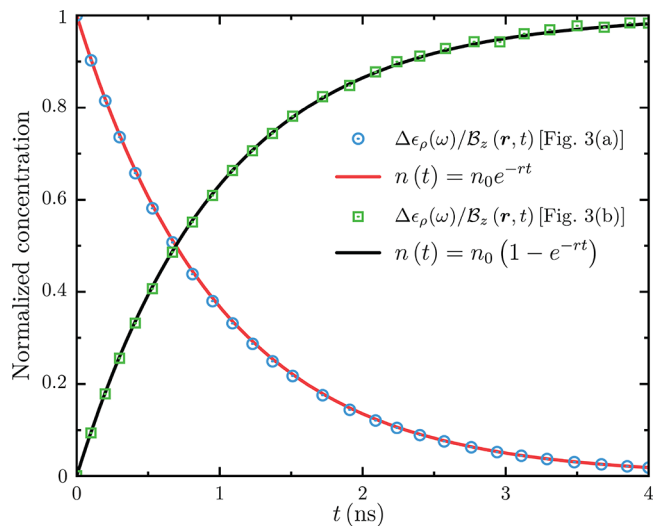


Figure 4. Real-time variations of ·OH radical concentration calculated by $\Delta\epsilon_r(\omega, \tau_c)/\mathcal{B}_z(r, t)$ for the two scenarios explored in Figure 3. The actual variations of $n(t)$ are also plotted for comparison. The frequency ω is fixed at $\omega = 34250 \text{ cm}^{-1}$. The other parameters adopted for the simulations are listed in section S3 in the SI.

Note that, in addition to the dynamic variation of molecular concentration at the nanosecond time scale, the proposed protocol may be conveniently generalized to the investigation of geometric and electronic dynamics of magnetic molecules or materials at the picosecond time scale, e.g., the ultrafast magnetization of ferromagnets triggered by a certain driving source.^{41,42} This can be achieved by adopting a picosecond pump AP VB in our protocol. Therefore, the time-resolved VBMCD protocol offers a useful spectroscopic tool for monitoring ultrafast dynamic processes of molecules.

To conclude, we have theoretically designed an efficient protocol for realizing the significantly enhanced magnet-free MCD measurement, where the strong longitudinal magnetic field of the nanosecond GHz AP VB induces the Zeeman splitting in the molecules, and the femtosecond UV–vis LCPL/RCPL enables the enhancement of the MCD signal. Furthermore, the time-resolved signal obtained by varying the pump–probe time delay promises to unravel transient molecular dynamics on the nanosecond time scale. The proposed protocol is currently feasible and may boost the investigation of ultrafast dynamic processes in magnetic molecules and materials.

ASSOCIATED CONTENT

Supporting Information

The Supporting Information is available free of charge at <https://pubs.acs.org/doi/10.1021/acs.jpclett.2c03370>.

Derivation of the formulas of the VBMCD spectrum, quantum chemistry calculations for the VBMCD spectrum of the ·OH radical, and parameters adopted for the simulations illustrated in Figures 2–4 (PDF)

AUTHOR INFORMATION

Corresponding Authors

Lyuzhou Ye – Hefei National Research Center for Physical Sciences at the Microscale, University of Science and Technology of China, Hefei, Anhui 230026, China;

orcid.org/0000-0001-8016-722X; Email: lzye@ustc.edu.cn

Xiao Zheng – Department of Chemistry, Fudan University, Shanghai 200433, China; orcid.org/0000-0002-9804-1833; Email: xzheng@fudan.edu.cn

Authors

Jiaan Cao – Hefei National Research Center for Physical Sciences at the Microscale, University of Science and Technology of China, Hefei, Anhui 230026, China

Dawei He – Hefei National Research Center for Physical Sciences at the Microscale, University of Science and Technology of China, Hefei, Anhui 230026, China

Shaul Mukamel – Department of Chemistry and Department of Physics and Astronomy, University of California, Irvine, California 92697, United States; orcid.org/0000-0002-6015-3135

Complete contact information is available at:
<https://pubs.acs.org/10.1021/acs.jpcllett.2c03370>

Author Contributions

J.C. and L.Y. contributed equally to this work.

Notes

The authors declare no competing financial interest.

ACKNOWLEDGMENTS

J.C., L.Y., D.H., and X.Z. acknowledge the support from the National Natural Science Foundation of China (Grant Nos. 21973086 and 22203083), the Fundamental Research Funds for the Central Universities (Grant No. WK2060000018), and the Ministry of Education of China (111 Project Grant No. B18051). S.M. was supported by the National Science Foundation (NSF) under Grant CHE-1953045, and the U.S. Department of Energy (DOE), Office of Science, Office of Basic Energy Sciences under Award Number DE-SC0022134. Computational resources are provided by the Supercomputing Center of University of Science and Technology of China.

REFERENCES

- Serrano, G.; Poggini, L.; Briganti, M.; Sorrentino, A. L.; Cucinotta, G.; Malavolti, L.; Cortigiani, B.; Otero, E.; Saintavit, P.; Loth, S.; et al. Quantum Dynamics of A Single Molecule Magnet on Superconducting Pb(111). *Nat. Mater.* **2020**, *19*, 546–551.
- Coronado, E. Molecular Magnetism: From Chemical Design to Spin Control in Molecules, Materials and Devices. *Nat. Rev. Mater.* **2020**, *5*, 87–104.
- Oh, I.; Park, J.; Choe, D.; Jo, J.; Jeong, H.; Jin, M.-J.; Jo, Y.; Suh, J.; Min, B.-C.; Yoo, J.-W. A Scalable Molecule-Based Magnetic Thin Film for Spin-Thermoelectric Energy Conversion. *Nat. Commun.* **2021**, *12*, 1–7.
- Zheng, Y.-Z.; Evangelisti, M.; Tuna, F.; Winpenny, R. E. Co–Ln Mixed-Metal Phosphonate Grids and Cages as Molecular Magnetic Refrigerants. *J. Am. Chem. Soc.* **2012**, *134*, 1057–1065.
- Richmond, C. J.; Miras, H. N.; De La Oliva, A. R.; Zang, H.; Sans, V.; Paramonov, L.; Makatsoris, C.; Inglis, R.; Brechin, E. K.; Long, D.-L.; et al. A Flow-System Array for the Discovery and Scale up of Inorganic Clusters. *Nat. Chem.* **2012**, *4*, 1037–1043.
- Karotsis, G.; Kennedy, S.; Teat, S. J.; Beavers, C. M.; Fowler, D. A.; Morales, J. J.; Evangelisti, M.; Dalgarno, S. J.; Brechin, E. K. $[Mn_4^{III}Ln_4^{III}]$ Calix[4]Arene Clusters as Enhanced Magnetic Coolers and Molecular Magnets. *J. Am. Chem. Soc.* **2010**, *132*, 12983–12990.
- Liu, S.-J.; Han, S.-D.; Zhao, J.-P.; Xu, J.; Bu, X.-H. In-Situ Synthesis of Molecular Magnetorefrigerant Materials. *Coord. Chem. Rev.* **2019**, *394*, 39–52.
- Chalkley, M. J.; Del Castillo, T. J.; Matson, B. D.; Peters, J. C. Fe-Mediated Nitrogen Fixation with a Metallocene Mediator: Exploring pK_a Effects and Demonstrating Electrocatalysis. *J. Am. Chem. Soc.* **2018**, *140*, 6122–6129.
- Nesbit, M. A.; Oyala, P. H.; Peters, J. C. Characterization of the Earliest Intermediate of Fe-N₂ Protonation: CW and Pulse EPR Detection of an Fe-NNH Species and its Evolution to Fe-NNH₂⁺. *J. Am. Chem. Soc.* **2019**, *141*, 8116–8127.
- Mason, W. R. *Magnetic Circular Dichroism Spectroscopy*; John Wiley & Sons: Inc.: Hoboken, NJ, 2007.
- Gonidec, M.; Davies, E. S.; McMaster, J.; Amabilino, D. B.; Veciana, J. Probing the Magnetic Properties of Three Interconvertible Redox States of a Single-Molecule Magnet with Magnetic Circular Dichroism Spectroscopy. *J. Am. Chem. Soc.* **2010**, *132*, 1756–1757.
- Toriumi, N.; Muranaka, A.; Kayahara, E.; Yamago, S.; Uchiyama, M. In-Plane Aromaticity in Cycloparaphenylen Dications: A Magnetic Circular Dichroism and Theoretical Study. *J. Am. Chem. Soc.* **2015**, *137*, 82–85.
- Han, B.; Gao, X.; Lv, J.; Tang, Z. Magnetic Circular Dichroism in Nanomaterials: New Opportunity in Understanding and Modulation of Excitonic and Plasmonic Resonances. *Adv. Mater.* **2020**, *32*, 1801491.
- Kjærgaard, T.; Coriani, S.; Ruud, K. Ab Initio Calculation of Magnetic Circular Dichroism. *WIREs Comput. Mol. Sci.* **2012**, *2*, 443–455.
- Yao, H. On the Electronic Structures of Au₂₅(SR)₁₈ Clusters Studied by Magnetic Circular Dichroism Spectroscopy. *J. Phys. Chem. Lett.* **2012**, *3*, 1701–1706.
- Daumann, L. J.; Tatum, D. S.; Snyder, B. E.; Ni, C.; Law, G.-I.; Solomon, E. I.; Raymond, K. N. New Insights into Structure and Luminescence of Eu^{III} and Sm^{III} Complexes of the 3,4,3-LI(1,2-HOPO) Ligand. *J. Am. Chem. Soc.* **2015**, *137*, 2816–2819.
- Kobayashi, N.; Muranaka, A. *Circular Dichroism and Magnetic Circular Dichroism Spectroscopy for Organic Chemists*; RSC Publishing: Cambridge, U.K., 2012.
- Heit, Y. N.; Sergent, D.-C.; Autschbach, J. Magnetic Circular Dichroism Spectra of Transition Metal Complexes Calculated from Restricted Active Space Wavefunctions. *Phys. Chem. Chem. Phys.* **2019**, *21*, 5586–5597.
- Guclu, C.; Veysi, M.; Capolino, F. Photoinduced Magnetic Nanoprobe Excited by an Azimuthally Polarized Vector Beam. *ACS Photonics* **2016**, *3*, 2049–2058.
- Mitić, N.; Saleh, L.; Schenk, G.; Bollinger, J. M.; Solomon, E. I. Rapid-Freeze-Quench Magnetic Circular Dichroism of Intermediate X in Ribonucleotide Reductase: New Structural Insight. *J. Am. Chem. Soc.* **2003**, *125*, 11200–11201.
- Snyder, R. A.; Bell, C. B., III; Diao, Y.; Krebs, C.; Bollinger, J. M., Jr.; Solomon, E. I. Circular Dichroism, Magnetic Circular Dichroism, and Variable Temperature Variable Field Magnetic Circular Dichroism Studies of Biferrous and Mixed-Valent myo-Inositol Oxygenase: Insights into Substrate Activation of O₂ Reactivity. *J. Am. Chem. Soc.* **2013**, *135*, 15851–15863.
- Daifuku, S. L.; Al-Afyouni, M. H.; Snyder, B. E.; Kneebone, J. L.; Neidig, M. L. A Combined Mössbauer, Magnetic Circular Dichroism, and Density Functional Theory Approach for Iron Cross-Coupling Catalysis: Electronic Structure, In Situ Formation, and Reactivity of Iron-Mesityl-Bisphosphines. *J. Am. Chem. Soc.* **2014**, *136*, 9132–9143.
- Tomita, M.; Murakami, M. High-Temperature Superconductor Bulk Magnets that can Trap Magnetic Fields of over 17 T at 29 K. *Nature* **2003**, *421*, 517–520.
- Durrell, J. H.; Dennis, A. R.; Jaroszynski, J.; Ainslie, M. D.; Palmer, K. G.; Shi, Y.; Campbell, A. M.; Hull, J.; Strasik, M.; Hellstrom, E.; et al. A Trapped Field of 17.6 T in Melt-Processed, Bulk Gd-Ba-Cu-O Reinforced with Shrink-Fit Steel. *Supercond. Sci. Technol.* **2014**, *27*, 082001.
- Ye, L.; Yang, L.; Zheng, X.; Mukamel, S. Enhancing Circular Dichroism Signals with Vector Beams. *Phys. Rev. Lett.* **2021**, *126*, 123001.

- (26) Zhan, Q. Cylindrical Vector Beams: From Mathematical Concepts to Applications. *Adv. Opt. Photonics* **2009**, *1*, 1–57.
- (27) Blanco, M.; Cambronero, F.; Flores-Arias, M. T.; Conejero Jarque, E.; Plaja, L.; Hernandez-Garcia, C. Ultraintense Femtosecond Magnetic Nanoprobes Induced by Azimuthally Polarized Laser Beams. *ACS Photonics* **2019**, *6*, 38–42.
- (28) Levy, U.; Silberberg, Y.; Davidson, N. Mathematics of Vectorial Gaussian Beams. *Adv. Opt. Photonics* **2019**, *11*, 828–891.
- (29) Rostov, V.; Romanchenko, I.; Pedos, M.; Rukin, S.; Sharypov, K.; Shpak, V.; Shunailov, S.; Ul'Masculov, M.; Yalandin, M. Superradiant Ka-Band Cherenkov Oscillator with 2-GW Peak Power. *Phys. Plasma* **2016**, *23*, 093103.
- (30) Mesyats, G.; Ginzburg, N.; Golovanov, A.; Denisov, G.; Romanchenko, I.; Rostov, V.; Sharypov, K.; Shpak, V.; Shunailov, S.; Ulmaskulov, M.; et al. Phase-Imposing Initiation of Cherenkov Superradiance Emission by an Ultrashort-Seed Microwave Pulse. *Phys. Rev. Lett.* **2017**, *118*, 264801.
- (31) Cho, M. *Two-Dimensional Optical Spectroscopy*; CRC Press: Boca Raton, 2009.
- (32) Mukamel, S. *Principles of Nonlinear Optical Spectroscopy*; Oxford University Press: New York, NY, 1995.
- (33) Lee, C.; Yang, W.; Parr, R. G. Development of the Colle-Salvetti Correlation-Energy Formula into a Functional of the Electron Density. *Phys. Rev. B* **1988**, *37*, 785.
- (34) Becke, A. D. Density-Functional Thermochemistry. V. Systematic Optimization of Exchange-Correlation Functionals. *J. Chem. Phys.* **1997**, *107*, 8554–8560.
- (35) Hehre, W. J.; Ditchfield, R.; Pople, J. A. Self-Consistent Molecular Orbital Methods. XII. Further Extensions of Gaussian-Type Basis Sets for Use in Molecular Orbital Studies of Organic Molecules. *J. Chem. Phys.* **1972**, *56*, 2257–2261.
- (36) Klene, M.; Robb, M. A.; Blancafort, L.; Frisch, M. J. A New Efficient Approach to the Direct Restricted Active Space Self-Consistent Field Method. *J. Chem. Phys.* **2003**, *119*, 713–728.
- (37) Dunning, T. H., Jr Gaussian Basis Sets for Use in Correlated Molecular Calculations. I. The Atoms Boron through Neon and Hydrogen. *J. Chem. Phys.* **1989**, *90*, 1007–1023.
- (38) Neese, F.; Wennmohs, F.; Becker, U.; Riplinger, C. The ORCA Quantum Chemistry Program Package. *J. Chem. Phys.* **2020**, *152*, 224108.
- (39) Aquilante, F.; Autschbach, J.; Carlson, R. K.; Chibotaru, L. F.; Delcey, M. G.; De Vico, L.; Galván, I. F.; Ferré, N.; Frutos, L. M.; Gagliardi, L.; et al. Molcas 8: New Capabilities for Multiconfigurational Quantum Chemical Calculations across the Periodic Table. *J. Comput. Chem.* **2016**, *37*, 506–541.
- (40) Berova, N.; Polavarapu, P. L.; Nakanishi, K.; Woody, R. W. *Comprehensive Chiroptical Spectroscopy: Instrumentation, Methodologies, and Theoretical Simulations*; John Wiley & Sons: Inc.: Hoboken, NJ, 2012; Vol.1.
- (41) Higley, D. J.; Hirsch, K.; Dakovski, G. L.; Jal, E.; Yuan, E.; Liu, T.; Lutman, A. A.; MacArthur, J. P.; Arenholz, E.; Chen, Z.; et al. Femtosecond X-Ray Magnetic Circular Dichroism Absorption Spectroscopy at an X-Ray Free Electron Laser. *Rev. Sci. Instrum.* **2016**, *87*, 033110.
- (42) Léveillé, C.; Burgos-Parra, E.; Sassi, Y.; Ajejas, F.; Chardonnet, V.; Pedersoli, E.; Capotondi, F.; De Ninno, G.; Maccherozzi, F.; Dhesi, S.; et al. Ultrafast Time-Evolution of Chiral Néel Magnetic Domain Walls Probed by Circular Dichroism in X-Ray Resonant Magnetic Scattering. *Nat. Commun.* **2022**, *13*, 1–6.

□ Recommended by ACS

All-Optical Noise Spectroscopy of a Solid-State Spin

Demity Farfurnik, Edo Waks, et al.

FEBRUARY 27, 2023

NANO LETTERS

READ ▶

Thermal Modulation of Magnetization Dynamics in Nanometer-Thick $L1_0$ -FePt Nanogranular and Continuous Films for High-Density Magnetic Recording Media

Yuta Sasaki, Yukiko K. Takahashi, et al.

MARCH 17, 2023

ACS APPLIED NANO MATERIALS

READ ▶

Role of Spin Transport through the β -Ta/ $Co_{20}Fe_{60}B_{20}$ Interface on its Ultrafast Demagnetization: Implications for Ultra-High-Speed Spin-Orbitronic Devices

Soma Dutta, Anjan Barman, et al.

DECEMBER 13, 2022

ACS APPLIED NANO MATERIALS

READ ▶

Insights into Magneto-Photocurrent and Coherent Spin Mixing for Binary and Ternary Nonfullerene Bulk Heterojunction Organic Solar Cells

Lixuan Kan, Kai Wang, et al.

NOVEMBER 09, 2022

CHEMISTRY OF MATERIALS

READ ▶

Get More Suggestions >

Supporting Information for

Magnet-Free Time-Resolved Magnetic Circular Dichroism with Pulsed Vector Beams

Jiaan Cao,^{1,*} Lyuzhou Ye,^{1,†} Dawei He,¹ Xiao Zheng,^{2,‡} and Shaul Mukamel³

¹*Hefei National Research Center for Physical Sciences at the Microscale,
University of Science and Technology of China, Hefei, Anhui 230026, China*

²*Department of Chemistry, Fudan University, Shanghai 200433, China*

³*Department of Chemistry and Department of Physics and Astronomy,
University of California, Irvine, California 92697, United States*

(Dated: November 30, 2022)

CONTENTS

Section S1. Derivation of the VBMCD signal	S2
Section S2. Quantum chemistry calculation on the ·OH radical	S5
Section S3. Parameters for simulations in Figures 2, 3, and 4 in the main text	S8
References	S9

Number of pages: 9

Number of tables: 7

* J.C. and L.Y. contributed equally to this work.

† lzye@ustc.edu.cn

‡ xzheng@fudan.edu.cn

Section S1. Derivation of the VBMCD signal

Using the first-order time-dependent perturbation theory, the electric polarization density at position \mathbf{r} is

$$\begin{aligned}\mathbf{P}(\mathbf{r}, t) &= n \text{Tr}[\hat{\mu} \rho^{(1)}(t)] \\ &= -n \frac{i}{\hbar} \int_{t_0}^t dt_1 \text{Tr}[\hat{\mu} \mathcal{G}_0(t, t_1) \mathcal{L}_{\text{int}}(\mathbf{r}, t_1) \mathcal{G}_0(t_1, t_0) \rho_0(t_0)]\end{aligned}\quad (\text{S1})$$

where n is the concentration of molecular sample, $\hat{\mu}$ is the electric transition dipole operator. \mathcal{G}_0 and \mathcal{L}_{int} are the propagator of the isolated molecule and the light-matter interaction operator in Liouville space, respectively. $\rho_0(t_0)$ represents the density matrix of isolated molecule. The corresponding magnetic polarization density is $\mathbf{M}(\mathbf{r}, t) = n \text{Tr}[\hat{m} \rho^{(1)}(t)]$, where \hat{m} is the magnetic transition dipole operator.

By solving the Maxwell equation,

$$\nabla^2 \mathbf{E}(\mathbf{r}, t) - \frac{1}{c^2} \frac{\partial^2 \mathbf{E}(\mathbf{r}, t)}{\partial t^2} = \mu_0 \frac{\partial^2 \mathbf{P}(\mathbf{r}, t)}{\partial t^2} + \mu_0 \frac{\partial \nabla \times \mathbf{M}(\mathbf{r}, t)}{\partial t}, \quad (\text{S2})$$

where μ_0 is the magnetic permeability, c is the light speed, and $\mathbf{E}(\mathbf{r}, t)$ is the electric field of the probe pulse. The resulting wavenumber k_j for the probe pulse ($j = \text{LCPL}$ and RCPL) after passing through the sample cuvette is

$$\begin{aligned}k_j(\omega) &= \frac{\omega}{c} - \frac{n\mu_0\omega c}{6\hbar N_g} \sum_{g_\alpha l_\beta} f_{l_\beta g_\alpha}(\omega) (\hat{\mu}_{l_\beta g_\alpha} \cdot \hat{\mu}_{g_\alpha l_\beta}) \\ &\quad \pm \frac{n\mu_0 c}{6\hbar^2} \left\{ \mathcal{B}_z(\mathbf{r}, t) [\tilde{A}(\omega; \Omega) + \tilde{B}(\omega; \Omega) + \tilde{C}(\omega; \Omega)] \right. \\ &\quad \left. + \mathcal{B}_z^*(\mathbf{r}, t) [\tilde{A}(\omega; -\Omega) + \tilde{B}(\omega; -\Omega) + \tilde{C}(\omega; -\Omega)] \right\},\end{aligned}\quad (\text{S3})$$

where N_g is the degeneracy of the ground state manifold and $\mathcal{B}_z(\mathbf{r}, t)$ is the longitudinal component of magnetic field of the pump, and $f_{l_\beta g_\alpha}(\omega) \equiv (\omega - \omega_{l_\beta g_\alpha} + i\eta)^{-1}$, with g_α and l_β labeling the states in the degenerate sublevels of the ground (g) and the excited (l) states, respectively. $\hat{\mu}_{l_\beta g_\alpha}$ and $\hat{m}_{l_\beta g_\alpha}$ denotes the electric and magnetic transition dipole moments between states l_β and g_α . In the second line, the plus/minus sign corresponds to the LCPL/RCPL pulse. The expressions of \tilde{A} , \tilde{B} , \tilde{C} are given in the main text.

Note that the wavenumber $k_j(\omega)$ (Equation S3) depends on the radial distance ρ and the pump central time T_c via the pump magnetic field $\mathcal{B}_z(\mathbf{r}, t)$. The linear absorption signal measured in radial ($\hat{\rho}$) direction is

$$I_\rho(\omega, \tau_c; k_j) = \frac{1}{\mu_0} \int dt \int_0^P \rho \mathbf{E}(\mathbf{r}, t) \times \mathbf{B}^*(\mathbf{r}, t) \cdot d\boldsymbol{\rho} + \text{c.c.} \quad (\text{S4})$$

$$\simeq \frac{\sqrt{2\pi}}{\ln 2} \frac{c\tau_d}{\mu_0 w_0^2} \left\{ \text{Im}[k_j(\omega, \tau_c; W_0)](F - Q) + \frac{2L}{w_0^2} F \right\}. \quad (\text{S5})$$

Here, P is the radius of interaction cross section between the probe beam and the sample cuvette and L is the path length of the cuvette; see Figure 1 of the main text. $k_j(\omega, \tau_c; W_0)$

is $k_j(\omega)$ (Equation S3) evaluated with $\rho = W_0$ and the central times of the pump and the probe pulses being T_c and t_c , respectively, and $\tau_c = t_c - T_c$ is the pump-probe time delay. F and Q are dimensionless functions of the reduced radius $\zeta_P \equiv P/w_0$ [1]:

$$\int_0^P d\rho |H(\mathbf{r})|^2 \simeq A_0^2 w_0^{-1} \left[\sqrt{\frac{2}{\pi}} \operatorname{erf} \left(\sqrt{2}\zeta_P \right) - \frac{4}{\pi} \zeta_P e^{-2\zeta_P^2} \right] \equiv w_0^{-1} Q(\zeta_P), \quad (\text{S6})$$

$$\int_0^P d\rho \rho^2 |H(\mathbf{r})|^2 \simeq A_0^2 w_0 \left[\frac{3}{2\sqrt{2\pi}} \operatorname{erf} \left(\sqrt{2}\zeta_P \right) - \frac{1}{\pi} \zeta_P e^{-2\zeta_P^2} (3 + 4\zeta_P^2) \right] \equiv w_0 F(\zeta_P). \quad (\text{S7})$$

The VBMCD signal detected along $\hat{\rho}$ is (see the main text for the definition of the absorption spectrum ϵ_ρ)

$$\Delta\epsilon_\rho(\omega, \tau_c) \equiv \epsilon_\rho(\omega, \tau_c; k_{\text{LCPL}}) - \epsilon_\rho(\omega, \tau_c; k_{\text{RCPL}}) \quad (\text{S8})$$

$$= \frac{1}{n_0 L} \ln \left[\frac{I_\rho(\omega, \tau_c; k_{\text{RCPL}})}{I_\rho(\omega, \tau_c; k_{\text{LCPL}})} \right] \quad (\text{S9})$$

$$\simeq \frac{2\operatorname{Im}[\Delta k(\omega, \tau_c; W_0)]}{n_0} \left(\frac{1}{4\zeta_L^2} \right) \left(\frac{Q}{F} - 1 \right) \quad (\text{S10})$$

$$\simeq \frac{\operatorname{Im}[\Delta \tilde{k}(\omega)]}{n_0} \frac{X(\tau_c)Y(\zeta_P)Z(\zeta_P)}{2\zeta_L^2}. \quad (\text{S11})$$

Here, n_0 is a reference molecular concentration, $Z(\zeta_P) \equiv Q/F - 1$ and $\Delta k(\omega, \tau_c; W_0) \equiv k_{\text{LCPL}}(\omega, \tau_c; W_0) - k_{\text{RCPL}}(\omega, \tau_c; W_0)$. From Equation S10 to S11, we have defined $\operatorname{Im}[\Delta \tilde{k}(\omega)] = \operatorname{Im}[\Delta k(\omega, \tau_c = 0; W_0)]$ and separated the temporal $[X(\tau_c)]$ and spatial $[Y(\zeta_P)]$ parts from $\operatorname{Im}[\Delta k(\omega, \tau_c; W_0)]$.

For comparison, we also give the expression of the conventional MCD with left- and right-circularly polarized (LCP and RCP) plane waves (PWs):

$$\Delta\epsilon_{\text{PW}}(\omega) \approx \frac{2\operatorname{Im}[\Delta k_{\text{PW}}(\omega)]}{n_0}. \quad (\text{S12})$$

Here, $\Delta k_{\text{PW}}(\omega) \equiv k_{\text{LCP}}(\omega) - k_{\text{RCP}}(\omega)$, and ($j = \text{LCP}$ and RCP)

$$k_j(\omega) = \frac{\omega}{c} - \frac{n\mu_0\omega c}{6\hbar N_g} \sum_{g_\alpha l_\beta} f_{l_\beta g_\alpha}(\omega) (\hat{\mu}_{l_\beta g_\alpha} \cdot \hat{\mu}_{g_\alpha l_\beta}) \pm \frac{n\mu_0 c}{6\hbar^2} B_z [A_{\text{PW}}(\omega) + B_{\text{PW}}(\omega) + C_{\text{PW}}(\omega)], \quad (\text{S13})$$

$$\Delta k_{\text{PW}}(\omega) = \frac{n\mu_0 c}{3\hbar^2} B_z [A_{\text{PW}}(\omega) + B_{\text{PW}}(\omega) + C_{\text{PW}}(\omega)], \quad (\text{S14})$$

where B_z is the static magnetic field applied along the \hat{z} direction, and in the second line of Equation S13 the plus/minus sign corresponds to the LCP/RCP beam. The A , B and C

terms read

$$A_{\text{PW}}(\omega) = \frac{i\omega}{2N_g} \sum_{g_\alpha, l_\beta} \sum_{g_{\alpha'}, l_{\beta'}} \frac{\partial f_{l_\beta g_\alpha}(\omega)}{\partial \omega} \left(\hat{\mathbf{m}}_{l_\beta l_{\beta'}} \delta_{g_\alpha g_{\alpha'}} - \hat{\mathbf{m}}_{g_\alpha g_{\alpha'}} \delta_{l_\beta l_{\beta'}} \right) \cdot \left(\hat{\boldsymbol{\mu}}_{g_{\alpha'} l_{\beta'}} \times \hat{\boldsymbol{\mu}}_{l_\beta g_\alpha} \right), \quad (\text{S15})$$

$$B_{\text{PW}}(\omega) = \frac{-i\omega}{N_g} \sum_{g_\alpha l_\beta} f_{l_\beta g_\alpha}(\omega) \left[\sum_{v_\gamma, v \neq g} \frac{(\hat{\boldsymbol{\mu}}_{l_\beta g_\alpha} \times \hat{\boldsymbol{\mu}}_{v_\gamma l_\beta}) \cdot \hat{\mathbf{m}}_{g_\alpha v_\gamma}}{\omega_{v_\gamma g_\alpha}} + \sum_{v_\gamma, v \neq l} \frac{(\hat{\boldsymbol{\mu}}_{g_\alpha v_\gamma} \times \hat{\boldsymbol{\mu}}_{l_\beta g_\alpha}) \cdot \hat{\mathbf{m}}_{v_\gamma l_\beta}}{\omega_{l_\beta v_\gamma}} \right], \quad (\text{S16})$$

$$C_{\text{PW}}(\omega) = \frac{-i}{2N_g} \frac{\hbar\omega}{k_B T} \sum_{g_\alpha, g_{\alpha'}, l_\beta} f_{l_\beta g_\alpha}(\omega) (\hat{\boldsymbol{\mu}}_{l_\beta g_\alpha} \times \hat{\boldsymbol{\mu}}_{g_{\alpha'} l_\beta}) \cdot \hat{\mathbf{m}}_{g_\alpha g_{\alpha'}}. \quad (\text{S17})$$

As mentioned in the main text, the peak value of the pump magnetic field \mathcal{B}_z can be further amplified to achieve a stronger VBMCD signal. For example, we adopt the following parameters for the VBMCD setup: the pump beam waist $W_0 = 1$ mm, the pump frequency $\Omega = 30$ GHz, the radius of interaction cross section $P = 0.13$ mm, and the length of sample cuvette $L = 0.1$ mm. Then as proposed in Ref. [2] by aiming the pump pulse to a metallic circular aperture with radius of $1\ \mu\text{m}$, the peak value of the pump magnetic field \mathcal{B}_z is amplified to 2.8 T [cf. Equation 3 of Ref. [2]], which is ~ 3.8 times stronger than that used in Figure 2d in the main text.

Section S2. Quantum chemistry calculation on the ·OH radical

The geometry of ·OH radical was optimized by using the density functional theory (DFT) method implemented in the ORCA program [3]. The hybrid exchange-correlation functional B3LYP [4, 5] was adopted with the use of the 6-31G basis set [6]. The optimized Cartesian atomic coordinates of ·OH radical are shown in Table S1.

The MOLCAS quantum chemistry software package [7] was then used to calculate the electronic states and electric/magnetic transition dipoles, at the restricted active space self-consistent field (RASSCF) level of theory [8] with all possible single and double excitations included. Specifically, the RASSCF(9,5)/aug-ccpVTZ [9] calculations were done using a state-average over the four lowest-lying valence states with equal weight. Table S2 shows the energies of the six lowest electronic states. Tables S3 and S4 show the electronic [$\mu \equiv (\mu_x, \mu_y, \mu_z)$] and magnetic [$\mathbf{m} \equiv (m_x, m_y, m_z)$] transition dipole moments, respectively.

TABLE S1. Optimized Cartesian coordinates x , y and z (in units of Å) of ·OH radical.

Atom	x (Å)	y (Å)	z (Å)
O	0.0000	0.0000	0.1108
H	0.0000	0.0000	-0.8861

TABLE S2. Energy information (in units of wavenumber cm⁻¹) of the six lowest electronic states of the ·OH radical.

State	Energy(cm ⁻¹)
1	0.0000
2	0.0000
3	131.1879
4	131.1879
5	34246.3077
6	34246.3077

TABLE S3. Electronic transition dipole moments [$\boldsymbol{\mu} \equiv (\mu_x, \mu_y, \mu_z)$] between states n and m in atomic units.

$n\ m$	$\langle n \hat{\mu}_x m\rangle$	$\langle n \hat{\mu}_y m\rangle$	$\langle n \hat{\mu}_z m\rangle$
1 1	0.00	0.00	-0.6612
1 2	0.00	0.00	0.00
1 3	0.00	0.00	0.00
1 4	-0.0002	$0.0002i$	0.00
1 5	-0.1094	$0.1094i$	0.00
1 6	0.00	0.00	0.00
2 2	0.00	0.00	-0.6612
2 3	0.0002	$0.0002i$	0.00
2 4	0.00	0.00	0.00
2 5	0.00	0.00	0.00
2 6	0.1094	$0.1094i$	0.00
3 3	0.00	0.00	-0.6612
3 4	0.00	0.00	0.00
3 5	$0.1082+0.0159i$	$-0.0159+0.1082i$	0.00
3 6	0.00	0.00	-0.0003
4 4	0.00	0.00	-0.6612
4 5	0.00	0.00	-0.0003
4 6	$-0.1082+0.0159i$	$0.0159+0.1082i$	0.00
5 5	0.00	0.00	-0.7547
5 6	0.00	0.00	0.00
6 6	0.00	0.00	-0.7547

TABLE S4. Magnetic transition dipole moments [$\mathbf{m} \equiv (m_x, m_y, m_z)$] between states n and m in atomic units.

n	m	$\langle n \hat{m}_x m \rangle$	$\langle n \hat{m}_y m \rangle$	$\langle n \hat{m}_z m \rangle$
1	1	0.00	0.00	1.00
1	2	0.00	0.00	0.00
1	3	0.00	0.00	0.00
1	4	0.0015	-0.0015 <i>i</i>	0.00
1	5	0.6782	-0.6782 <i>i</i>	0.00
1	6	0.00	0.00	0.00
2	2	0.00	0.00	-1.00
2	3	0.0015	0.0015 <i>i</i>	0.00
2	4	0.00	0.00	0.00
2	5	0.00	0.00	0.00
2	6	0.6782	0.6782 <i>i</i>	0.00
3	3	0.00	0.00	-1.00
3	4	0.0029+0.0004 <i>i</i>	-0.0004+0.0029 <i>i</i>	0.00
3	5	0.6711+0.0986 <i>i</i>	-0.0986+0.6711 <i>i</i>	0.00
3	6	0.00	0.00	0.0022
4	4	0.00	0.00	1.00
4	5	0.00	0.00	-0.0022
4	6	0.6711-0.0986 <i>i</i>	-0.0986-0.6711 <i>i</i>	0.00
5	5	0.00	0.00	0.000005
5	6	-0.0029+0.0004 <i>i</i>	0.0004+0.0029 <i>i</i>	0.00
6	6	0.00	0.00	-0.000005

Section S3. Parameters for simulations in Figures 2, 3, and 4 in the main text

TABLE S5. Parameters adopted in Figure 2 in the main text.

	Parameters
Figure 2a and b	$\Omega = 30 \text{ GHz}$, $W_0 = 1 \text{ mm}$, $A_0 = 27.2 \text{ kV}$, $\tau_D = 0.66 \text{ ns}$, $T_c = 1 \text{ ns}$, $\omega = 34250 \text{ cm}^{-1}$, $w_0 = 1 \text{ mm}$, $A_0 = 27.2 \text{ V}$, $\tau_d = 6.66 \text{ fs}$, $\zeta_L = 0.1$, $n = n_0 = 10^{-7} \text{ mol} \cdot \text{L}^{-1}$, $T = 1.73 \text{ K}$. The peak powers of pump and probe are 14 MW and 10 W, respectively.
Figure 2c	$\rho = 0.1 \text{ mm}$, $\tau_c = 0.13 \text{ ns}$. The other parameters are the same as those in Figure 2a.
Figure 2d	For $\text{Im}[\Delta\tilde{k}(\omega)]$ and $\text{Im}[\Delta k_{\text{PW}}(\omega)]$: $\rho = 1 \text{ mm}$, $\tau_c = 0$, $B_z = 0.1 \text{ T}$. For $\Delta\epsilon_\rho(\omega)$ and $\Delta\epsilon_{\text{PW}}(\omega)$: $\zeta_P = 0.13$, $\tau_c = 0.13 \text{ ns}$, $B_z = 7.4 \text{ T}$. The other parameters are the same as those in Figure 2a.

TABLE S6. Parameters adopted in Figure 3 in the main text.

	Parameters
Figure 3	$\Omega = 30 \text{ GHz}$, $W_0 = 1 \text{ mm}$, $A_0 = 27.2 \text{ kV}$, $\tau_D = 0.66 \text{ ns}$, $w_0 = 1 \text{ mm}$, $A_0 = 27.2 \text{ V}$, $\tau_d = 6.66 \text{ fs}$, $\zeta_P = 0.13$, $\zeta_L = 0.1$, $n_0 = 10^{-7} \text{ mol} \cdot \text{L}^{-1}$, $T = 1.73 \text{ K}$. The peak powers of pump and probe are 14 MW and 10 W, respectively.

TABLE S7. Parameters adopted in Figure 4 in the main text.

	Parameters
Figure 4	$\Omega = 30 \text{ GHz}$, $W_0 = 1 \text{ mm}$, $A_0 = 27.2 \text{ kV}$, $\tau_D = 0.66 \text{ ns}$, $w_0 = 1 \text{ mm}$, $A_0 = 27.2 \text{ V}$, $\tau_d = 6.66 \text{ fs}$, $P = 0.13 \text{ mm}$, $L = 0.1 \text{ mm}$, $\zeta_P = 0.13$, $\zeta_L = 0.1$, $n_0 = 10^{-7} \text{ mol} \cdot \text{L}^{-1}$, $T = 1.73 \text{ K}$. The peak powers of pump and probe are 14 MW and 10 W, respectively.

REFERENCES

- [1] Ye, L.; Yang, L.; Zheng, X.; Mukamel, S. Enhancing Circular Dichroism Signals with Vector Beams. *Phys. Rev. Lett.* **2021**, *126*, 123001.
- [2] Blanco, M.; Cambronero, F.; Flores-Arias, M. T.; Conejero Jarque, E.; Plaja, L.; Hernandez-Garcia, C. Ultraintense Femtosecond Magnetic Nanoprobes Induced by Azimuthally Polarized Laser Beams. *ACS Photonics* **2019**, *6*, 38–42.
- [3] Neese, F.; Wennmohs, F.; Becker, U.; Ripplinger, C. The ORCA Quantum Chemistry Program Package. *J. Chem. Phys. C* **2020**, *152*, 224108.
- [4] Lee, C.; Yang, W.; Parr, R. G. Development of the Colle-Salvetti Correlation-Energy Formula into a Functional of the Electron Density. *Phys. Rev. B* **1988**, *37*, 785.
- [5] Becke, A. D. Density-Functional Thermochemistry. V. Systematic Optimization of Exchange-Correlation Functionals. *J. Chem. Phys.* **1997**, *107*, 8554–8560.
- [6] Hehre, W. J.; Ditchfield, R.; Pople, J. A. Self-Consistent Molecular Orbital Methods. XII. Further Extensions of Gaussian-Type Basis Sets for Use in Molecular Orbital Studies of Organic Molecules. *J. Chem. Phys.* **1972**, *56*, 2257–2261.
- [7] Aquilante, F.; Autschbach, J.; Carlson, R. K.; Chibotaru, L. F.; Delcey, M. G.; De Vico, L.; Fdez. Galván, I.; Ferré, N.; Frutos, L. M.; Gagliardi, L., et al. Molcas 8: New Capabilities for Multiconfigurational Quantum Chemical Calculations across the Periodic Table. *J. Comput. Chem.* **2016**, *37*, 506–541.
- [8] Klene, M.; Robb, M. A.; Blancafort, L.; Frisch, M. J. A New Efficient Approach to the Direct Restricted Active Space Self-Consistent Field Method. *J. Chem. Phys.* **2003**, *119*, 713–728.
- [9] Dunning Jr, T. H. Gaussian Basis Sets for Use in Correlated Molecular Calculations. I. The Atoms Boron through Neon and Hydrogen. *J. Chem. Phys.* **1989**, *90*, 1007–1023.